# Electronic Supporting Information (ESI)

## Porous network of boron-doped $IrO_2$ nanoneedles with enhanced mass activity for acidic oxygen evolution reactions

Fei Hu,*[a] Peiyu Huang,[a] Xu Feng,[a] Changjian Zhou,[a] Xinjuan Zeng,[a] Congcong Liu,[c]

Guangjin Wang,*[a] Xiaowei Yang *[b] and Huawen Hu*[a]

[a] *School of Materials Science and Hydrogen Energy, Foshan University, Foshan, 528000, P.R. China*

[b] *School of Chemistry and Chemical Engineering, Shanghai Jiao Tong University, Shanghai 200240, P.R. China*

[c] *Flexible Electronics Innovation Institute (FEII), Jiangxi Science and Technology Normal University, Nanchang 330013, P.R. China*

* Corresponding authors' email addresses: mfhufei@fosu.edu.cn; huawenhu@126.com; wgj501@163.com; yangxw@sjtu.edu.cn

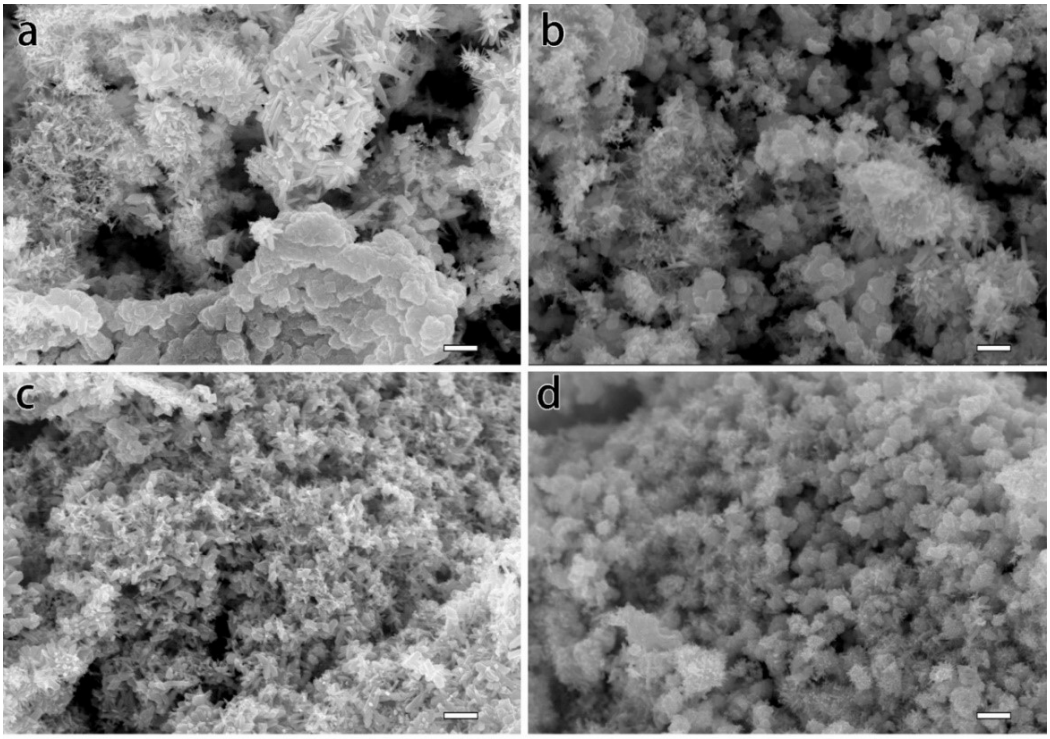


**Figure S1. a-d**) SEM images of the $IrO_2$ samples prepared with different structure-shaping agents. (**a**) and (**b**) correspond to the samples prepared using chloride ions as the structure-shaping agent, while (**c**) and (**d**) involve the use of a mixture of chloride ions and cysteamine hydrochloride as the structure-shaping agent. Scale bars in (**a-d**): 400 nm.

We selected typical chloride ions and cysteamine hydrochloride as the structure-shaping agent (i.e., capping agent) for the anisotropic growth of $IrO_2$, given their strong adsorptive nature. In our preliminary experiments, we confirmed that chloride ions could function as structure-shaping agents, facilitating the formation of nanorod morphologies when used in appropriate amounts (see **Figure S1a**, and **S1b**). Additionally, we explored the combined effects of both chloride ions and cysteamine hydrochloride on the $IrO_2$ morphology variation. The coexistence of chloride ions and cysteamine hydrochloride results in enhanced uniformity of the produced nanorods or nanoneedles (please see **Figure S1c** and **d**). However, the exclusive use of cysteamine hydrochloride allowed the highest uniformity among the generated nanoneedles that intertwine into a porous network. Therefore, we selected cysteamine hydrochloride as the structure-shaping agent for the preparation of the porous network of $IrO_2$ nanoneedles. Cysteamine hydrochloride acts as a capping agent, adsorbing onto specific facets and altering the surface energy of the

$IrO_2$-cysteamine complex. This causes the crystal to preferentially grow along the <101> direction, resulting in a nanoneedle morphology with a small tip diameter (*Mater. Lett.*, 2012, **68**, 153-156).

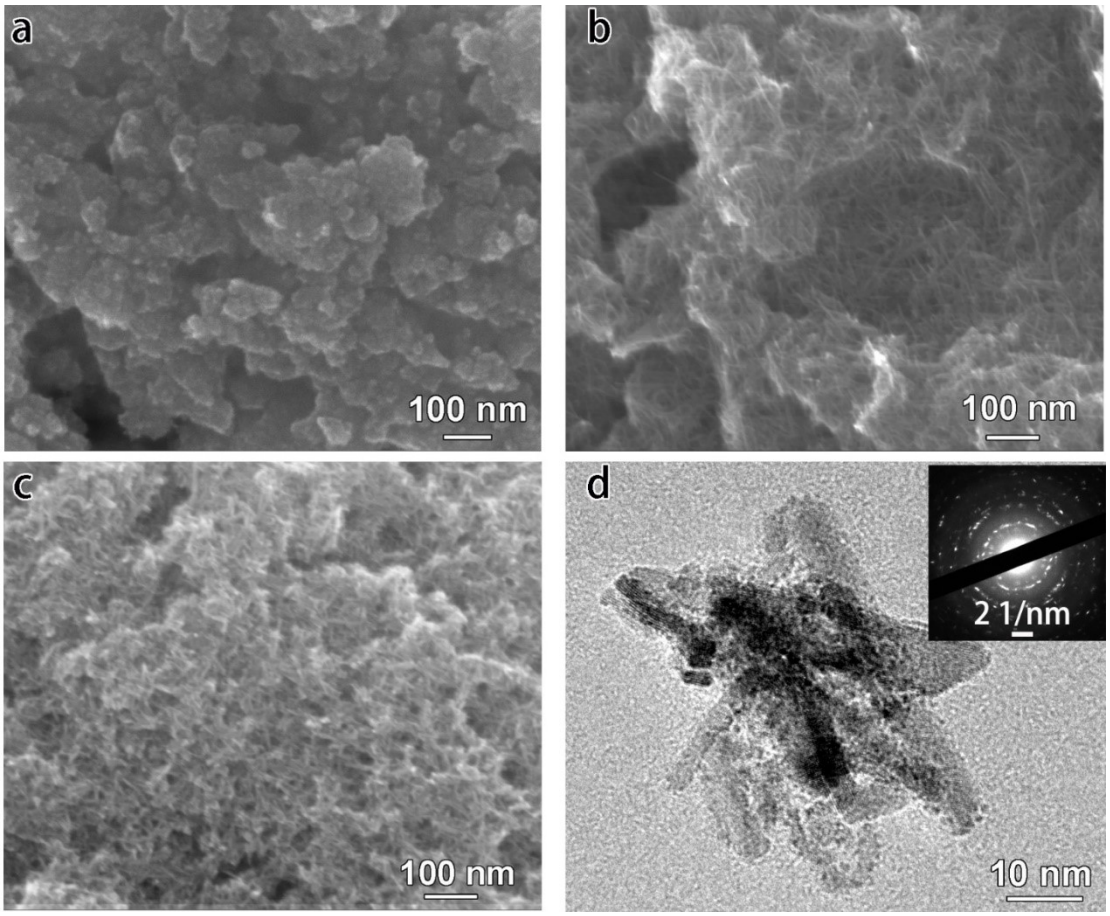


**Figure S2. a-c**) SEM images of A-$IrO_2$ (**a**) and B-$IrO_2$ (**b**), and L-$IrO_2$ (**c**). (**d**) TEM image of L-$IrO_2$.

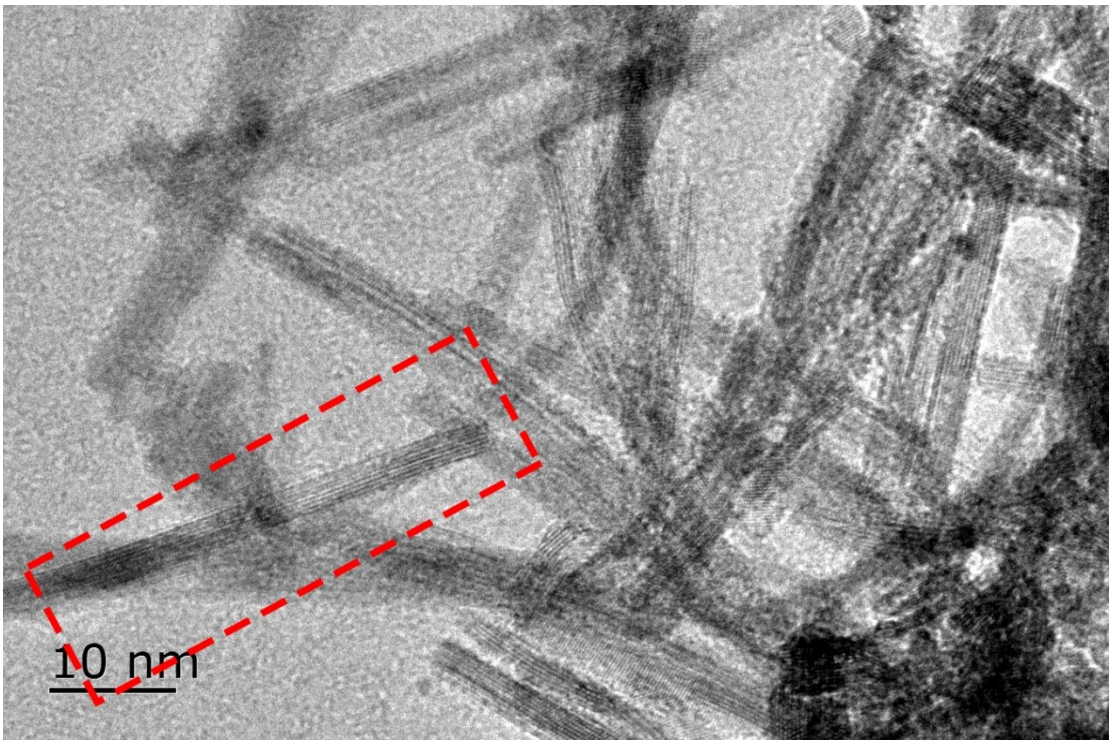


**Figure S3.** The original TEM image of B-$IrO_2$. The red dashed rectangle highlights the region displayed in **Figure 2c**.

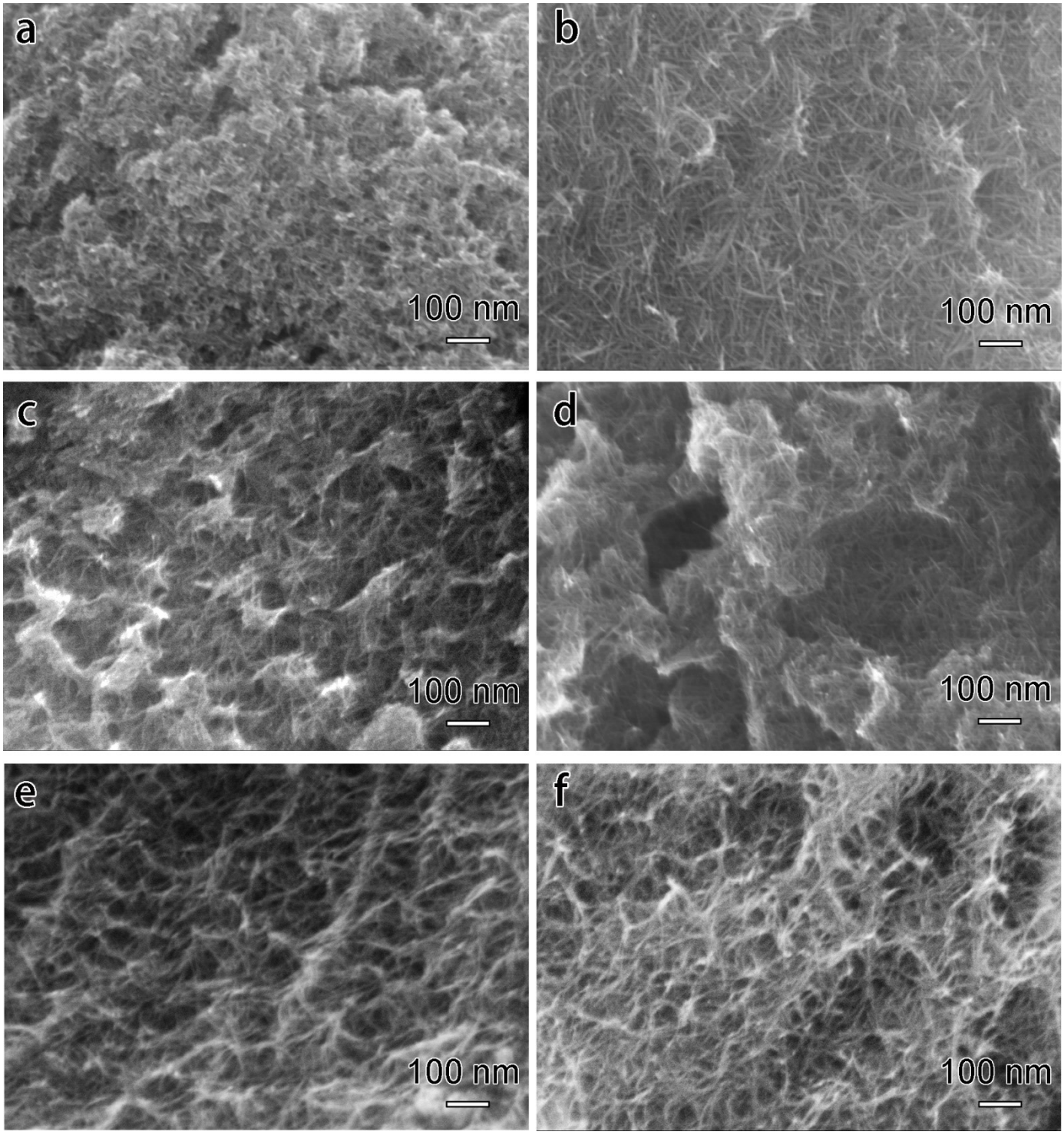


**Figure S4. a-f**) SEM images of porous networks of $IrO_2$ and B-$IrO_2$ nanoneedles synthesized at the B/Ir atomic ratios of 0 (**a**), 3 (**b**), 5 (**c**), 8 (**d**), 11 (**e**), and 13 (**f**).

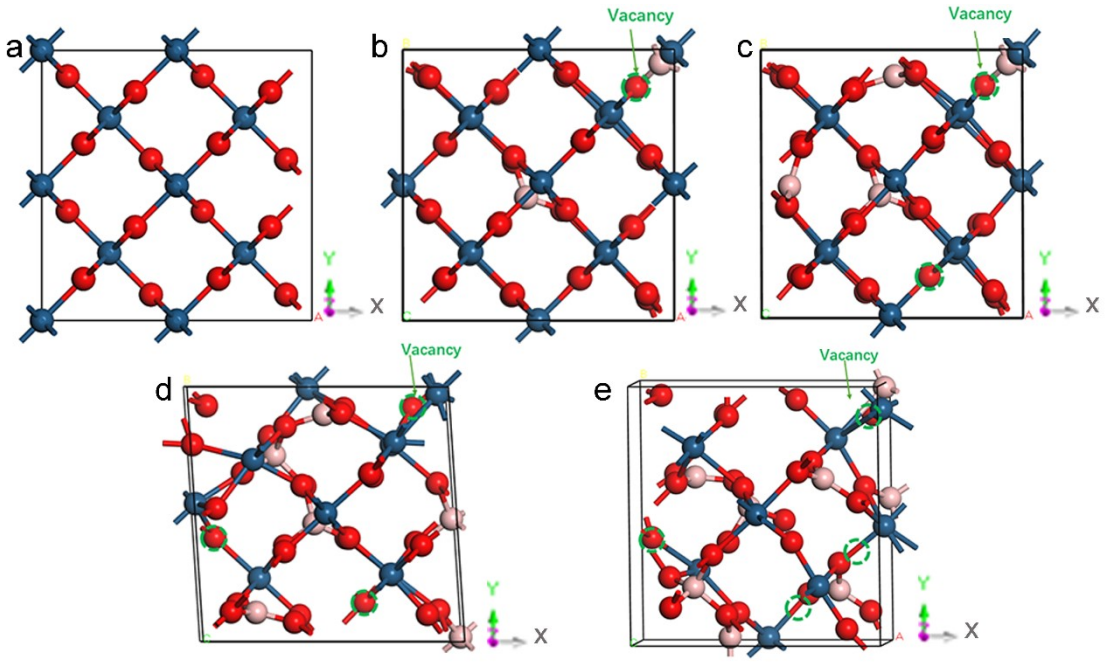


**Figure S5.** The optimized configurations of $IrO_2$ and B-$IrO_2$ constructed by doping 2, 4, 6 and 8 boron atoms based on DFT computations. Red, blue, and pink spheres represent oxygen, iridium, and boron atoms, respectively.

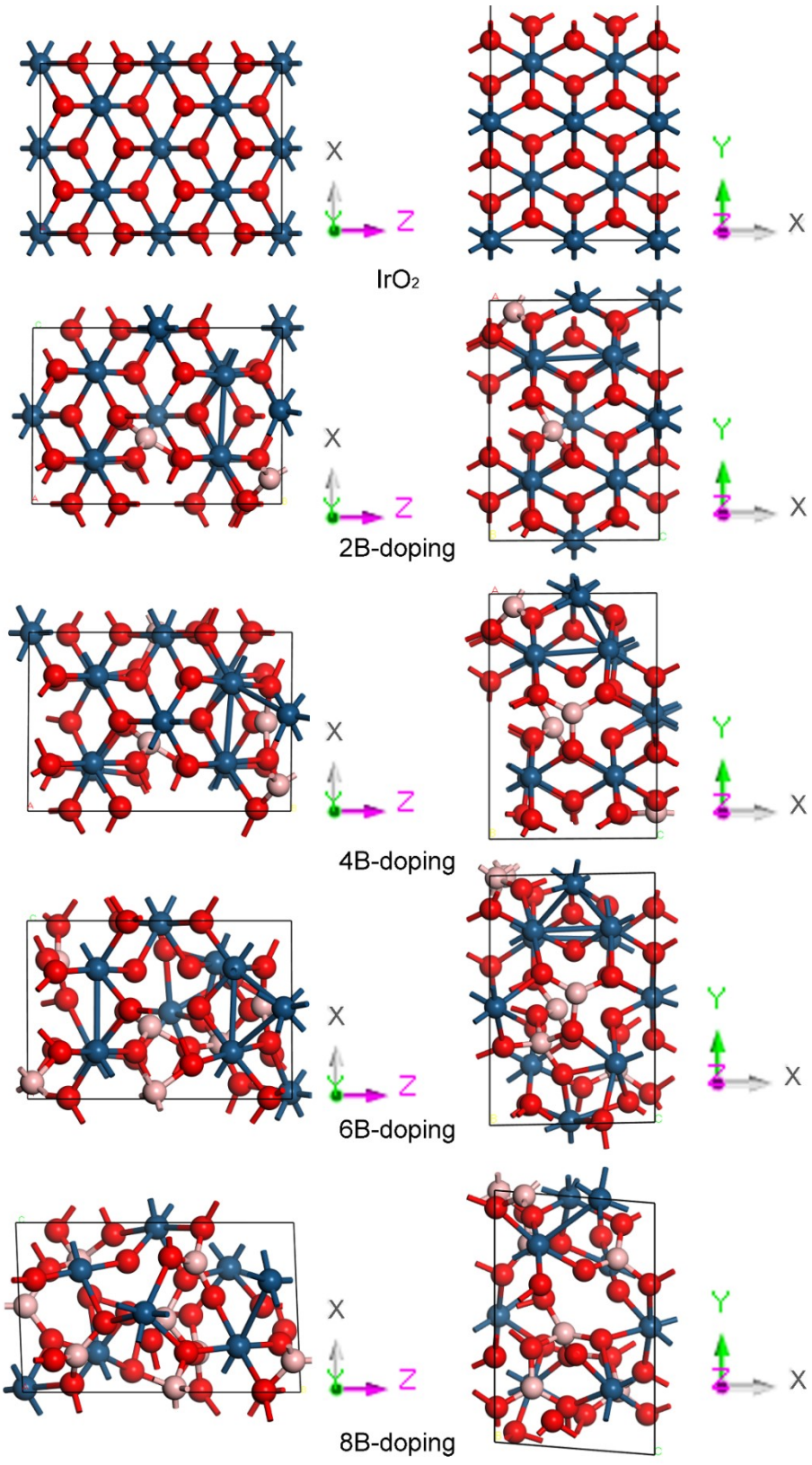


**Figure S6.** Observing the optimized configurations of $IrO_2$ and B-$IrO_2$ constructed by doping 2, 4, 6, and 8 boron atoms at different viewing angles based on DFT computations. Red, blue, and pink spheres represent oxygen, iridium, and boron atoms, respectively.

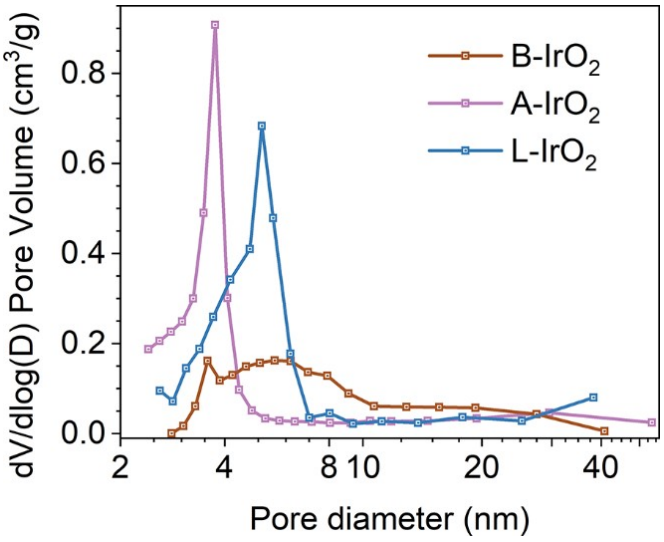


**Figure S7.** BJH pore size distribution plots depicted based on the desorption branch of the $N_2$ physisorption isotherms of the A-$IrO_2$, L-$IrO_2$, and B-$IrO_2$ samples.

When A-$IrO_2$ nanoparticles are transformed into L-$IrO_2$ and B-$IrO_2$ nanoneedle networks, the mesopore content increases, as evidenced by a more pronounced hysteresis loop. Additionally, B doping promotes further $IrO_2$ anisotropic crystallite growth, reducing the micropore content to some extent. Similar $N_2$ adsorption isotherms were observed for $IrO_2$-based granules (*Nat. Commun.*, 2023, **14**, 1248; *Sci. China Mater.*, 2021, **64**, 2958-2966.) and nanoneedles (*Adv. Funct. Mater.*, 2017, **28**, 1704796; *Nat. Commun.*, 2023, **14**, 1248). The total pore volumes, micropore volumes, and BJH pore size distribution of these samples were summarized in **Table S1** and **Figure S7**. The pores in A-$IrO_2$ are primarily concentrated below 4 nm, whereas B-$IrO_2$ contains larger pores up to 10 nm. It is recognized that micropores significantly contribute to the specific surface area, as supported by references [48, 49] in the revised manuscript (*Adv. Energ. Mater.*, 2011, **1**, 678-683; *Energy Fuels*, 2023, **37**, 8284-8295). A-$IrO_2$ exhibits a micropore volume of 0.5159 $cm^3 \cdot g^{-1}$, which is two orders of magnitude higher than that of B-$IrO_2$ (0.0042 $cm^3 \cdot g^{-1}$).

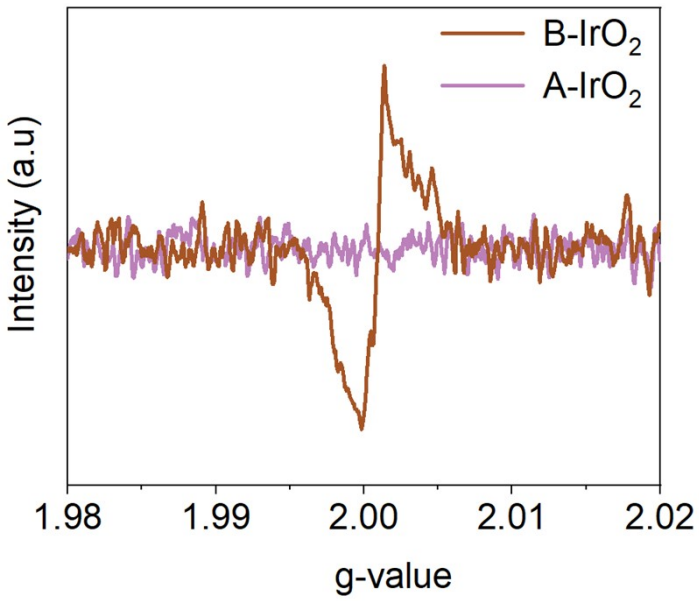


**Figure S8.** EPR spectra of the A-$IrO_2$ and B-$IrO_2$ samples.

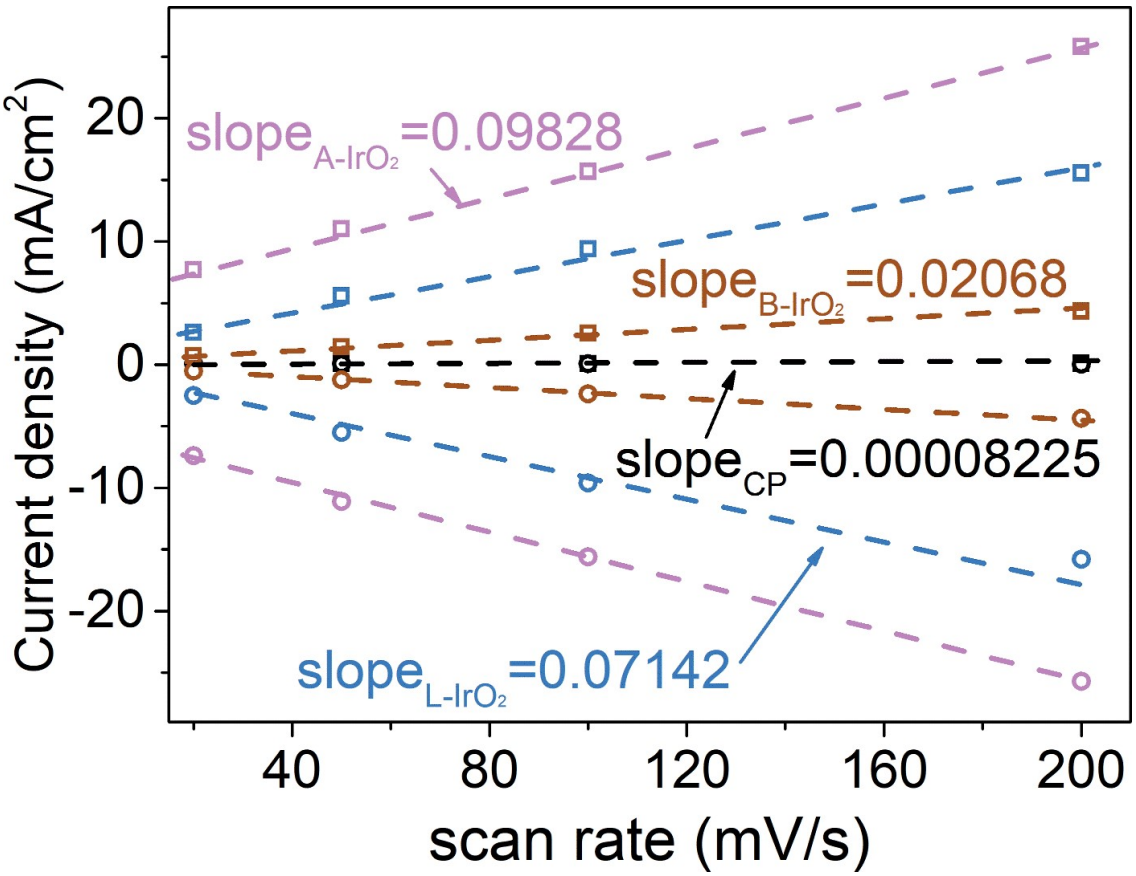


**Figure S9.** The current density against the scan rate of B-$IrO_2$, L-$IrO_2$, A-$IrO_2$, and CP in the non-faradaic current regions. The $C_{dl}$ values of B-$IrO_2$, L-$IrO_2$, and A-$IrO_2$ were calculated as 10.34, 35.76, and 49.14 mF·cm$^{-2}$, respectively. Thus, the corresponding ECSAs of B-$IrO_2$, L-$IrO_2$, and A-$IrO_2$ were calculated as 344.6, 1192, and 1638, respectively.

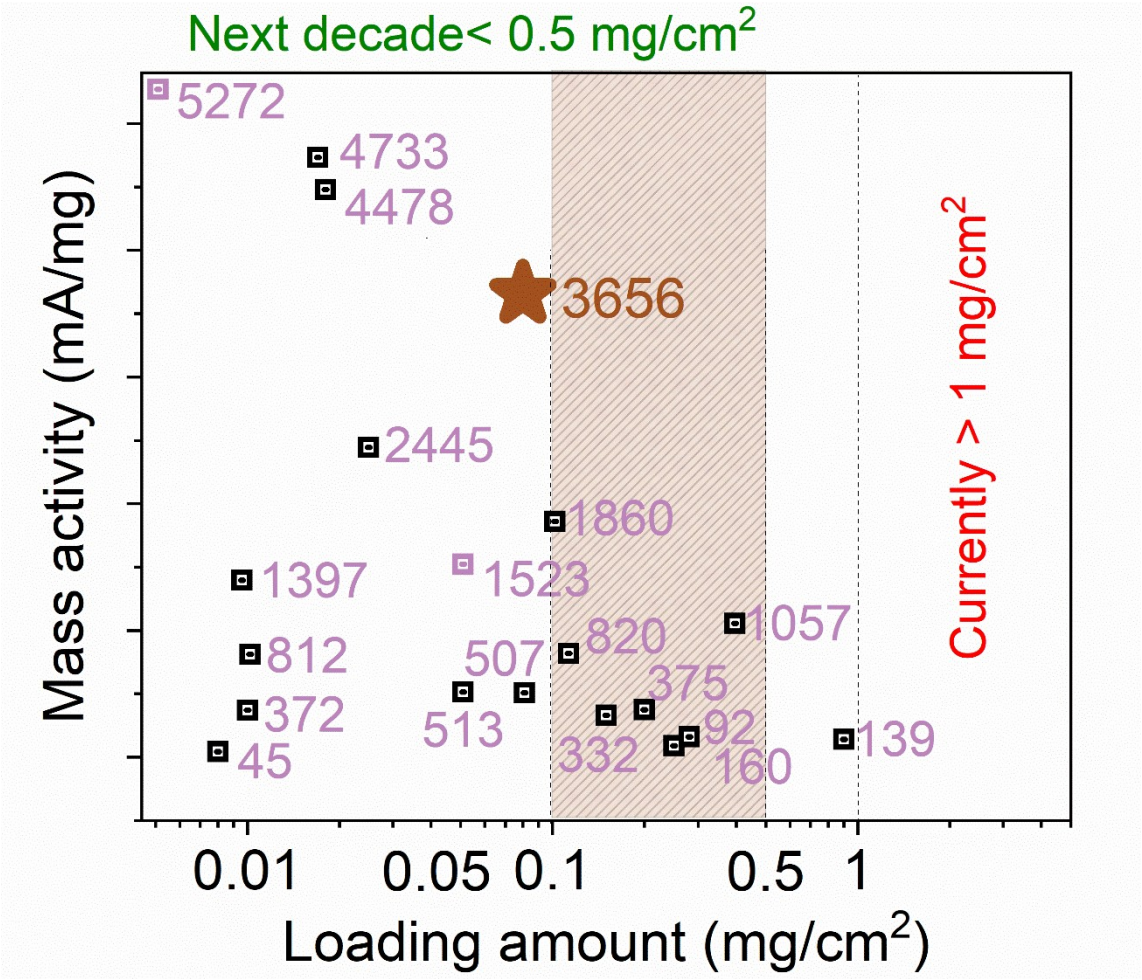


**Figure S10.** Comparison of the mass activity of our B-$IrO_2$ (indicated by an asterisk) with those of previously reported Ir-based anodes. For comparison with that of B-$IrO_2$, the mass activities at 1.55 $V_{RHE}$ were extracted from the related references (please refer to the updated **Table S3** with more examples). Currently, the loading amount of the Ir catalyst is higher than 1 mg/cm$^2$. The dashed area represents the Department of Energy (DOE)'s target, which aims to reduce Ir loading to below 0.5 mg/cm$^2$ and 0.1 mg/cm$^2$, corresponding to projected advancements of up to 20 GW/a and 100 GW/a, respectively.

Mass activity measured using a half-cell setup may not accurately reflect the performance of a PEMWE cell, as the mass loading of Ir in PEMWE systems is generally greater than 1 mg/cm$^2$ due to the considerations related to anode preparation and the lifetime of the PEMWE [Science 384 (2024) 666-670; Adv. Mater. 36 (2024) 2402643; Adv. Mater. 36 (2024) 2314049; J. Am. Chem. Soc. 146 (2024) 7858-7867]. Our PEMWE incorporating 0.08 $mg_{Ir}/cm^2$ of B-$IrO_2$ possessed the mass activities to be 3625 and 10025 $mA \cdot mg_{Ir}^{-1}$ at cell voltages of 1.6 and 1.9 V, respectively.

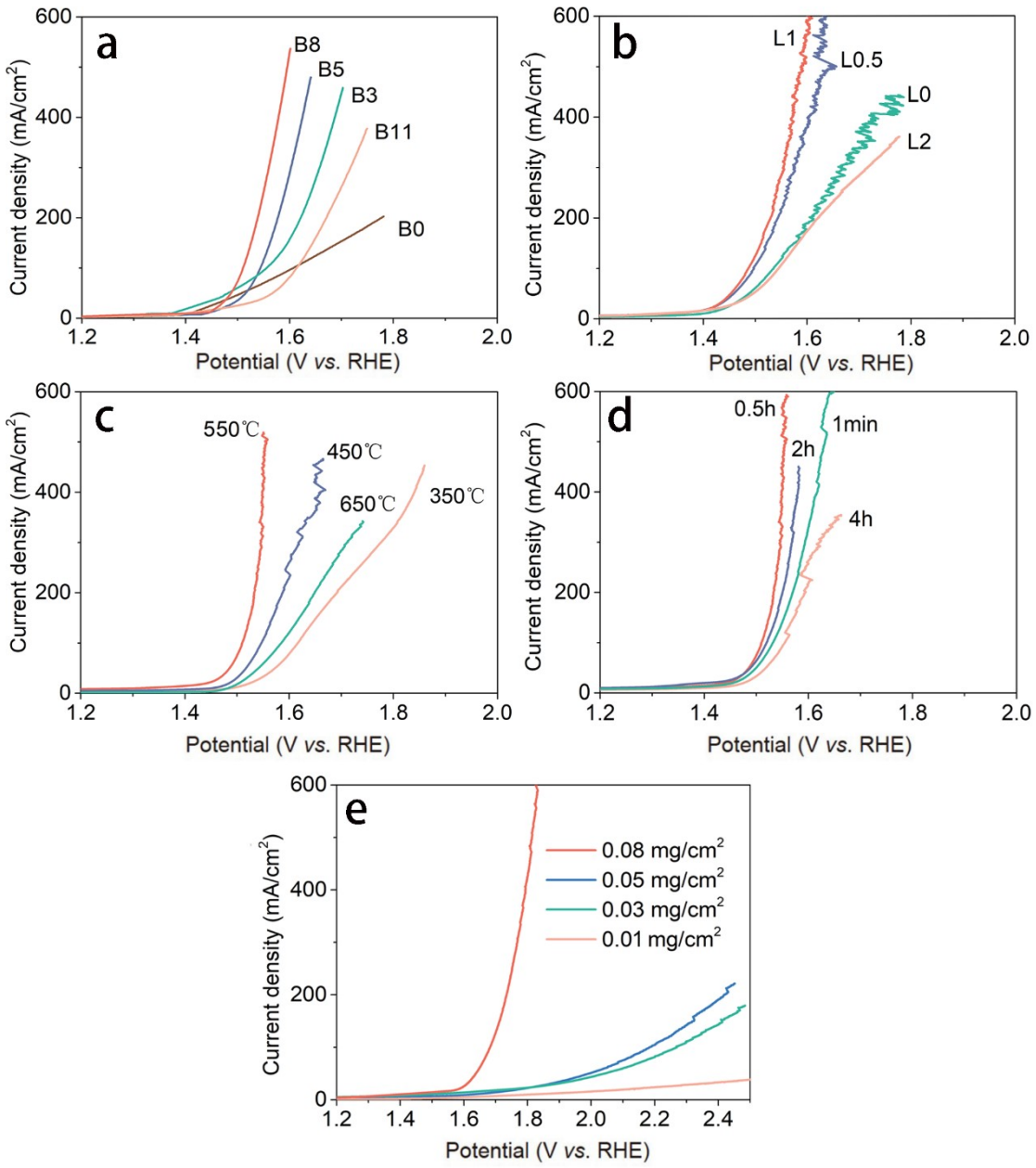


**Figure S11. a-e**) Effects of boron contents in precursors (**a**), cysteamine·HCl contents in precursors (**b**), calcination temperatures (**c**), holding durations (**d**), and loading amounts (**e**) on the OER performance of B-doped $IrO_2$.

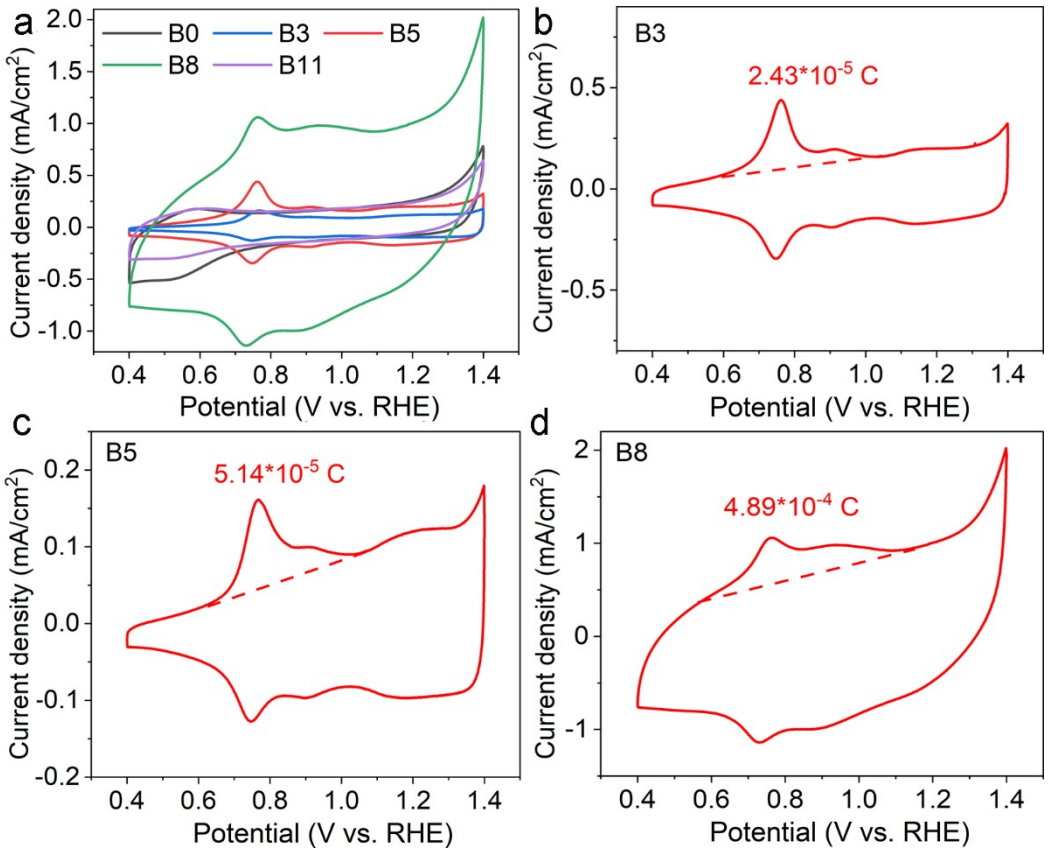


**Figure S12.** (**a**) Overlapped CV curves of a series of B-doped $IrO_2$ samples bearing different B doping extents (including B3, B5, B8, and B11) for measuring their active Ir sites. (**b-d**) Single CV curves of different B-doped $IrO_2$ samples, including B3 (**b**), B5 (**c**), and B8 (**d**). Note that redox peaks can barely be observed in (**a**) for the B11 sample with excessive B doping. It can be noted that the B8 (namely B-$IrO_2$) sample exhibits the greatest number of electrochemically active Ir sites.

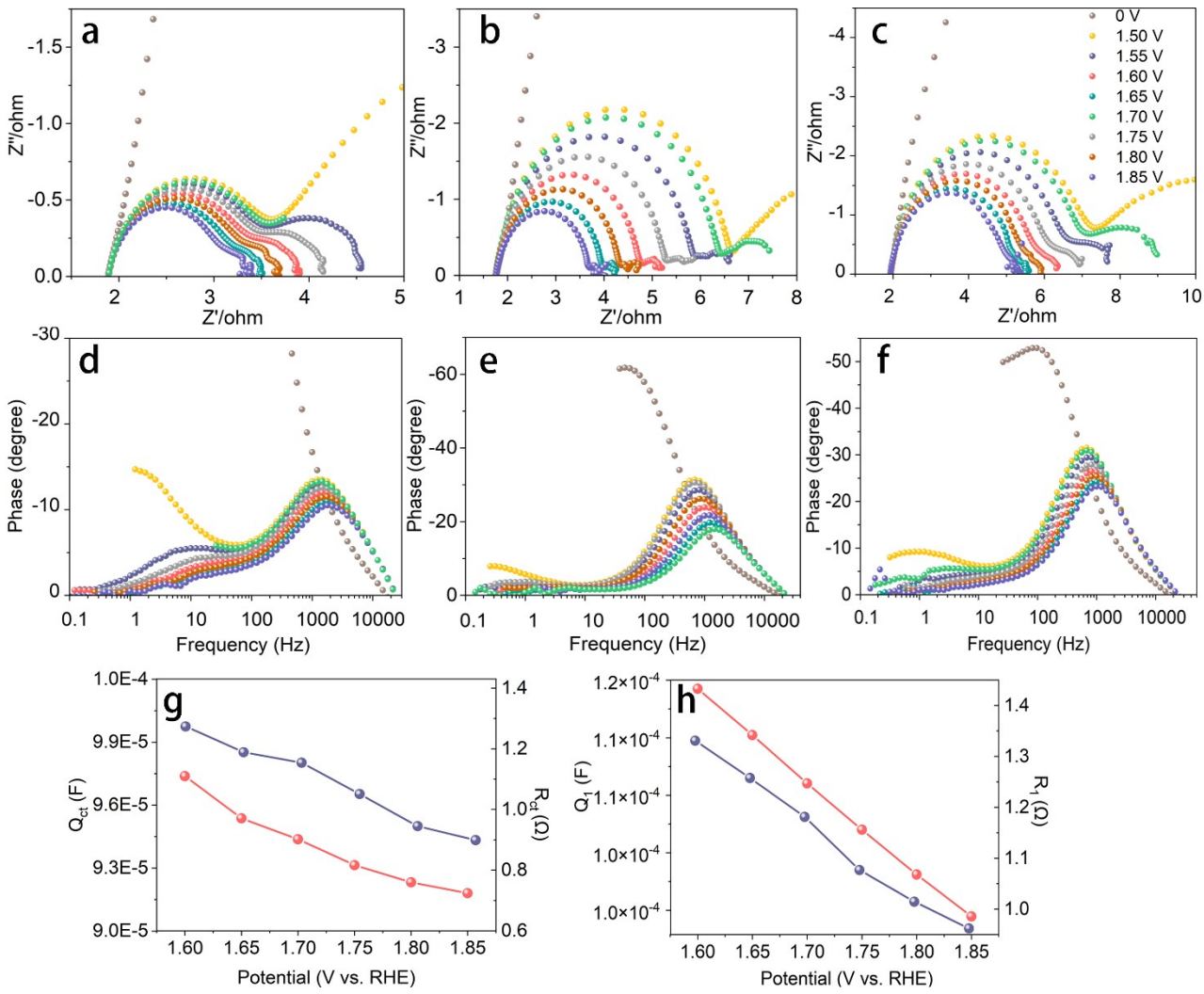


**Figure S13. a-f**) Nyquist plots (a-c), and Bode plots (d-f) of A-$IrO_2$ (**a, d**), L-$IrO_2$ (**b, e**), and B-$IrO_2$ (**c, f**) at different potentials. (**g, h**) The optimum fitting values of $R_{ct}$ and $Q_{ct}$ (**g**) and $R_1$ and $Q_1$ (**h**) plotted as a function of applied potentials for B-$IrO_2$.

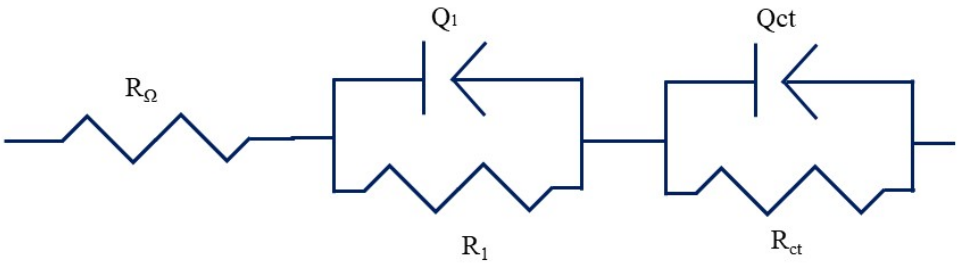


**Figure S14.** Equivalent circuit used for fitting the impedance data presented in **Figure S13a**.

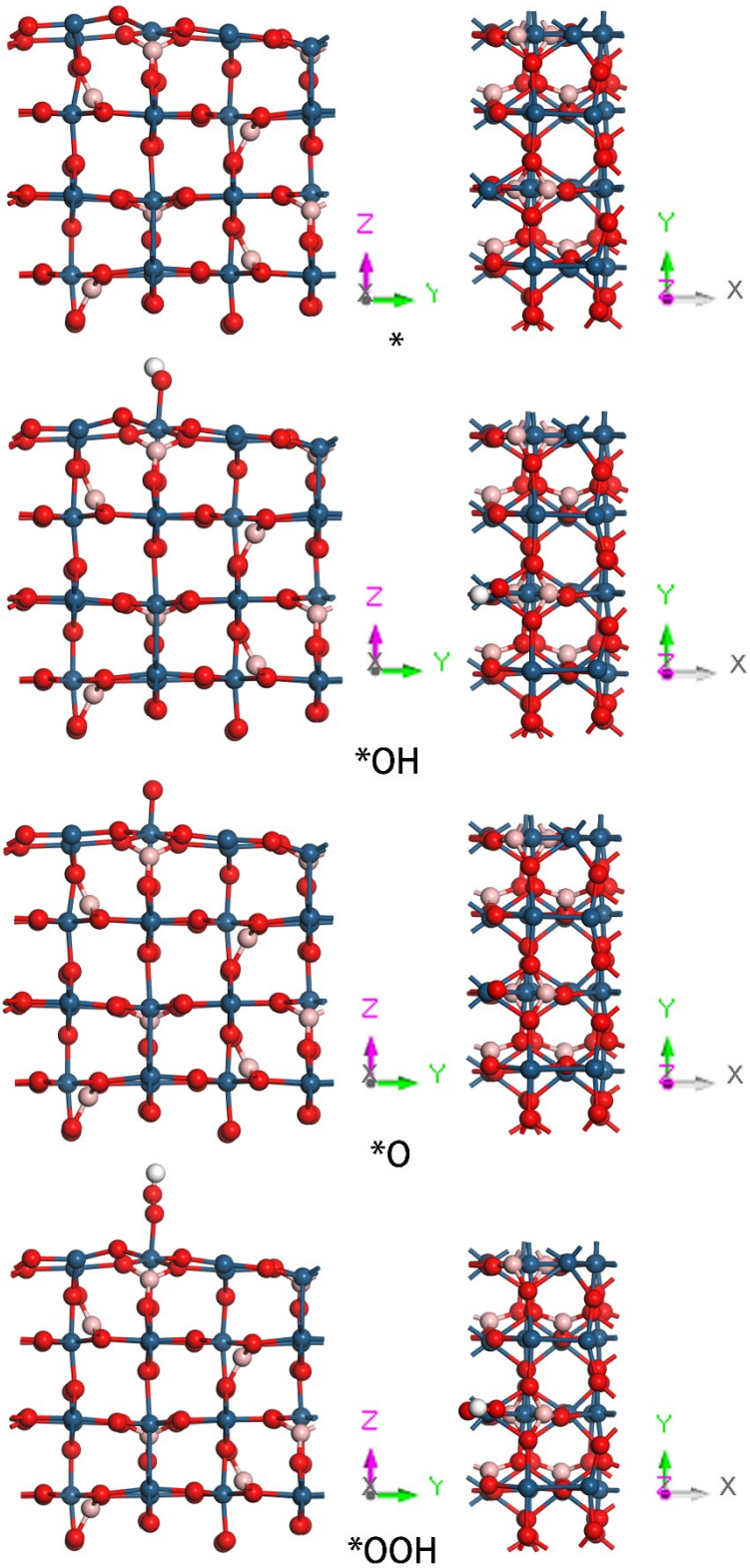


**Figure S15.** The optimized atomic models for OER intermediates on B-$IrO_2$: (a) side view, (b) top view.

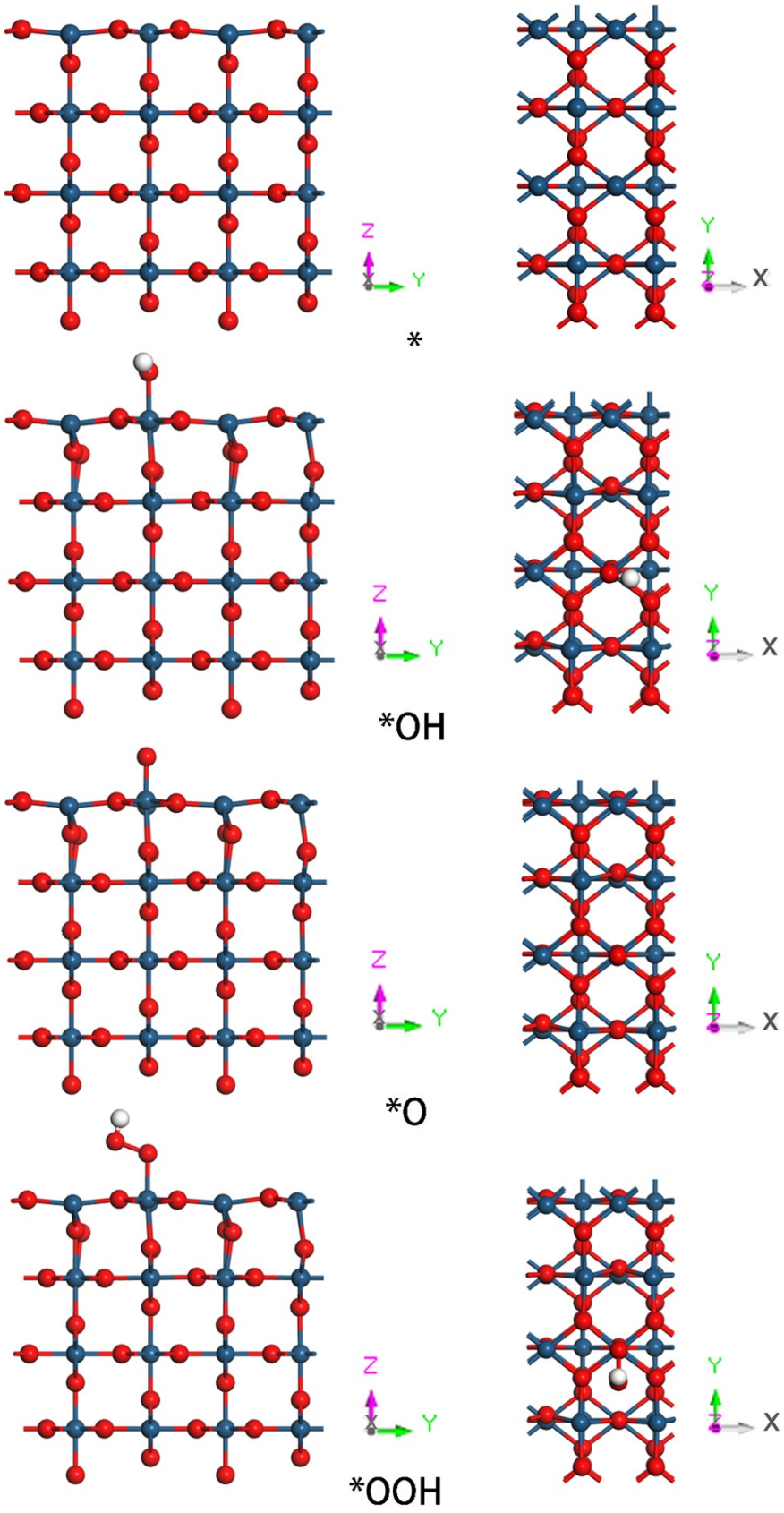


**Figure S16.** The optimized atomic models for OER intermediates on $IrO_2$: (a) side view, (b) top view.

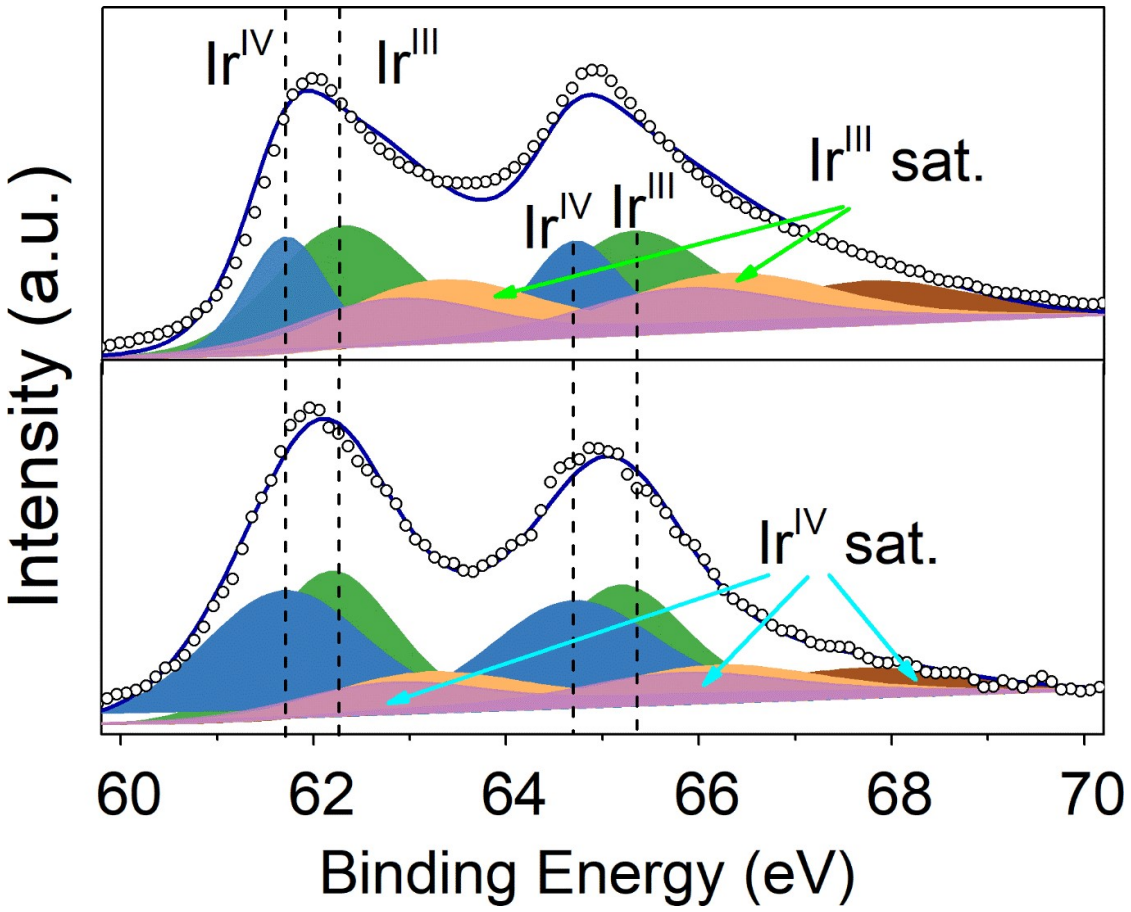


**Figure S17.** Ir 4f XPS spectra for B-$IrO_2$ before and after the stability test.

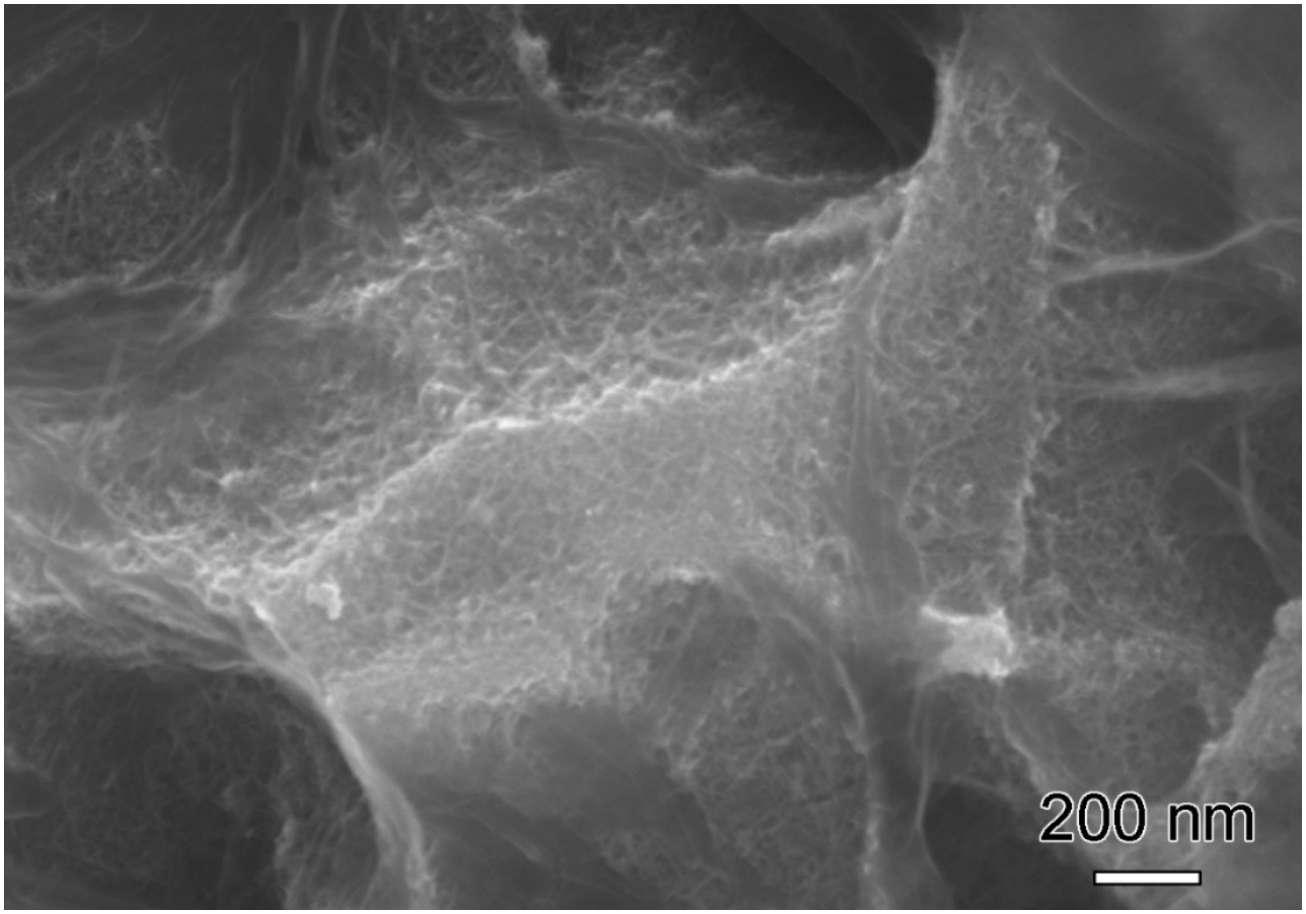


**Figure S18.** SEM image showing the distinct structure of B-$IrO_2$ on the Ti-felt substrate.

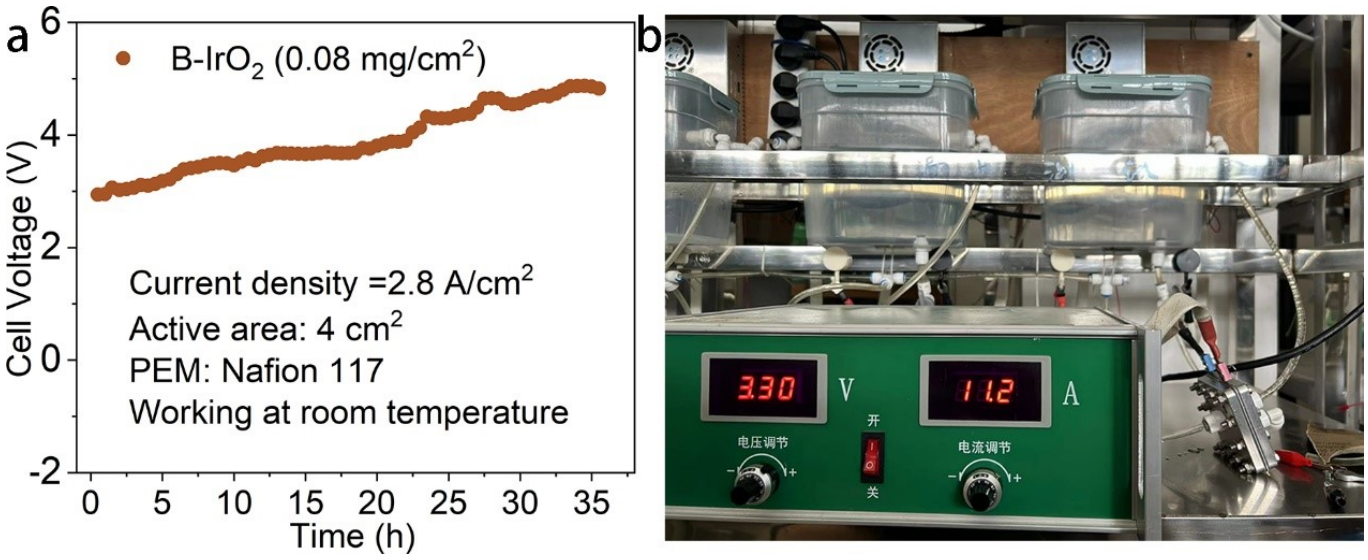


**Figure S19.** (**a**) Static durability test of the B-$IrO_2$ catalyst in a PEMWE single cell by galvanostatic operation at 2.8 A·$cm^2$ for 35 h. (**b**) On-site observation of the operation current and voltage after running for 5 h.

The rapid proton transfer in the PEMWE system is advantageous for achieving high current density output. However, it presents a challenge for anodic catalysts. To evaluate the stability of the B-$IrO_2$ catalyst, we conducted a static durability test at a current density of 2.8 A·$cm^{-2}$ for 35 h. The operation began at 2.98 V and remained stable within 4.00 V for the first 24 h, after which the cell voltage increased rapidly. During the operation, the cell was slightly heated up. **Figure S19** illustrates the operation current and voltage after running for 5 h. Overall, the voltage during operation at 2.8 A·$cm^{-2}$ remains significantly high and is thus far from practical utilization. The performance of our PEMWE with B-$IrO_2$ can be further improved by meticulous adjustments to the gas diffusion layers (GDLs), catalyst-coated membrane (CCM), gas and fluid channels, and other components.

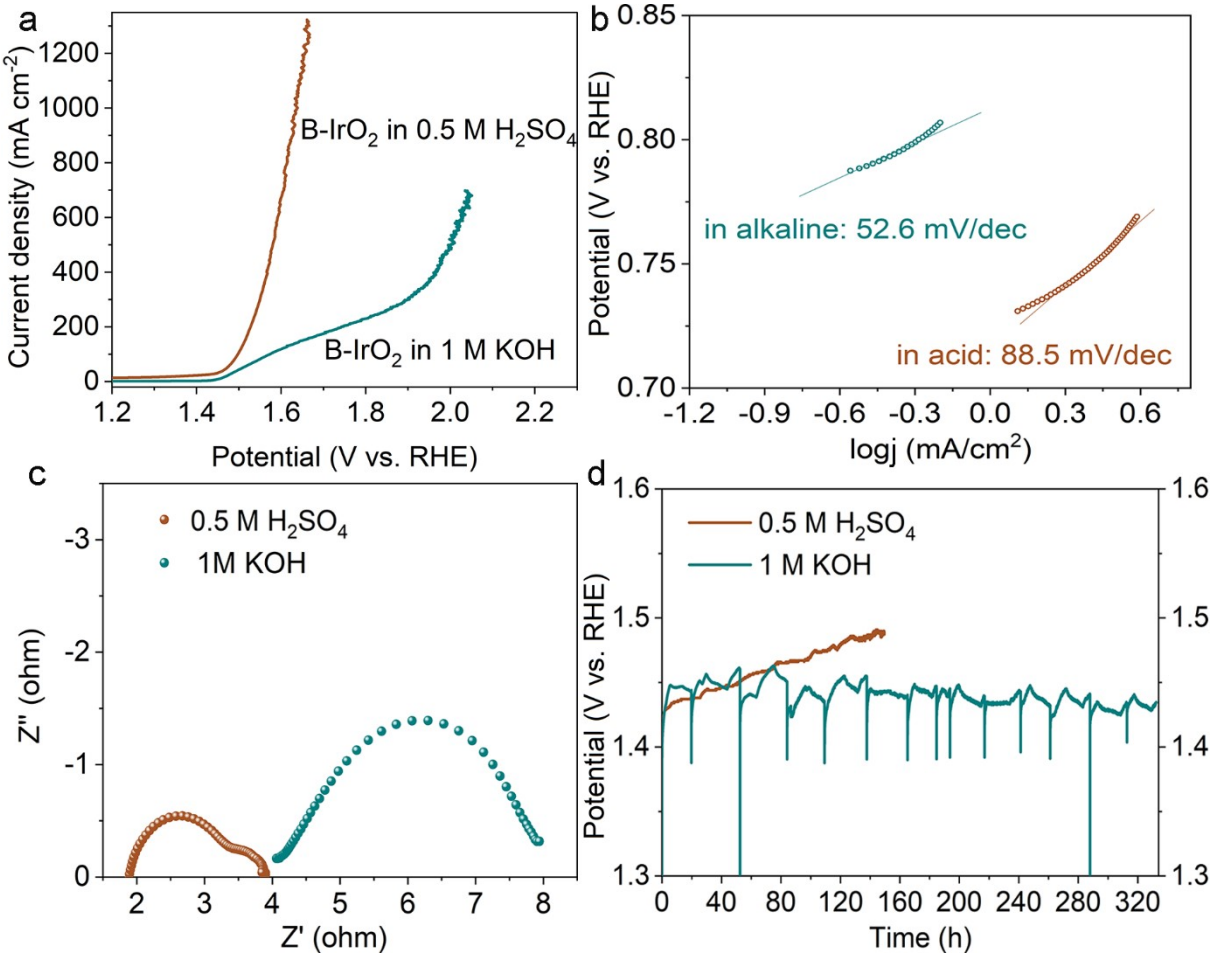


**Figure S20. Electrochemical OER performance of B-$IrO_2$ in 1 M KOH and 0.5 M $H_2SO_4$ electrolytes**. (**a**) Polarization curves recorded at a scanning rate of 5 mV·$s^{-1}$. (**b**) Tafel plots derived from the polarization curves shown in (**a**). (**c**) Nyquist plots of samples recorded at 1.5 $V_{RHE}$. (**d**) Chronopotentiometric measurements conducted at 10 mA·$cm^{-2}$.

**Table S1.** Summary of the total pore volumes and micropore volumes of the A-$IrO_2$, L-$IrO_2$, and B-$IrO_2$ samples.

| Parameter \ Sample | **A-$IrO_2$** | **L-$IrO_2$** | **B-$IrO_2$** |
|---|---|---|---|
| Total pore volume ($cm^3 \cdot g^{-1}$) | 0.1609 | 0.2171 | 0.0995 |
| t-Plot micropore volume ($cm^3 \cdot g^{-1}$) | 0.5159 | 0.0409 | 0.0042 |

**Table S2.** Comparison of the performance of our B-$IrO_2$ with recently reported B-doped or incorporated $IrO_2$-based electrocatalysts for OER.

| Electrocatalysts | Electrolyte | $\eta@j_{10}$, mV | $\eta@j_{100}$, mV | Mass activity @1.55 $V_{RHE}$ | Stability | Ref. |
|---|---|---|---|---|---|---|
| **B-$IrO_2$** | **0.5 M $H_2SO_4$** | **218** | **268** | **3656.3 mA·mg$^{-1}$ at the Ir loading of 0.08 $mg_{Ir}/cm^2$** | **150 h @10 mA·cm$^{-2}$ & 160 h @ 1 A·cm$^{-2}$ for cell** | **This work** |
| B-doped amorphous iridium oxide ($IrO_x$-B) | 0.1 M $HClO_4$ | 255~292 | / | 1523.2 to 5271.6 mA·mg$^{-1}$ with the Ir loading from 51 to 5.1 $\mu g_{Ir}/cm^2$ | 10 h @10 mA·cm$^{-2}$ | Sci. China Mater. 64 (2021) 2958-2966 |
| B-incorporated $IrO_2$-$Ta_2O_5$ ($B_{0.6}$-$IrO_2$-$Ta_2O_5$/Ti) | 0.5 M $H_2SO_4$ | 210 | 264 | / | 400 h @100 mA·cm$^{-2}$ | Chem. Eng. J. 491 (2024) 152040 |
| Nanoporous high-entropy catalysts doped with B | $Al_{94}Co_1Cu_1Fe_1Mo_1Ni_1B_1$ | 295 | ~380 | / | / | Nanoscale 16 (2024) 4803-4810 |
| | 1.0 M KOH | | | | | |
| | $Al_{93}Co_1Cu_1Fe_1Mo_1Ni_1Ir_1B_1$ | 277 | ~350 | / | 55 h @100 mA·cm$^{-2}$ | |
| Ir/$B_4C$ | 0.1 M $HClO_4$ | 283 | / | 1396.7 mA·mg$^{-1}$ | 180 min @10 mA·cm$^{-2}$ | J. Power Sources 512 (2021) 230506 |
| IrWB nanochannels | 0.5 M $H_2SO_4$ | 291 | 350 | / | 800 h @100 mA·cm$^{-2}$ | Nat. Commun. 12 (2021) 3540 |

Note: η stands for the overpotential.

**Table S3.** Mass activities of Ir-based OER electrocatalysts under acidic conditions reported recently.

| Electrocatalysts | $\eta@j_{10}$ (mV) | Mass activity | Mass activity @1.55 $V_{RHE}$ | Electrolyte | Loading amount | Ref. |
|---|---|---|---|---|---|---|
| **B-$IrO_2$** | **210** | **2589.1** mA·mg$^{-1}$ **@1.53 $V_{RHE}$** | **3656.3** mA·mg$^{-1}$ | **0.5 M $H_2SO_4$** | **0.08 $mg_{Ir}/cm^2$** | **This work** |
| Co-doped $SrIrO_3$ | 245 | ~1700 mA·mg$^{-1}$ @1.53 $V_{RHE}$ | 2445.3 mA·mg$^{-1}$ | 0.5 M $H_2SO_4$ | 0.025 mg/cm$^2$ | Nat. Commun.15 (2024) 2928 |
| $Ir_3Ni$ | 282 | 3720 mA·$mg_{Ir}^{-1}$ @1.58 $V_{RHE}$ | 1860 mA·$mg_{Ir}^{-1}$ | 0.2 M $HClO_4$ | 0.102 mg/cm$^2$ | J. Am. Chem. Soc. 146(2024)7858−7867 |
| Ir/$WO_3$/CC | 249 | 2858 mA·mg$^{-1}$ @1.53 $V_{RHE}$ | 4732.7 mA·mg$^{-1}$ | 0.5 M $H_2SO_4$ | 0.017 mg/cm$^2$ | Angew. Chem. Int. Ed. (2024) e202406947 |
| IrRuNiMoCo | 243 | 261.5 mA·$mg_{Ir}^{-1}$ @1.53 $V_{RHE}$ | 332.1 mA·$mg_{Ir}^{-1}$ | 0.5 M $H_2SO_4$ | 0.15 mg/cm$^2$ | Adv. Mater. 36 (2024) 2314049 |
| Ir-Ce SSO | 238 | 637.88 mA·mg$^{-1}$ @1.55 $V_{RHE}$ | 1057.3 mA·mg$^{-1}$ | 0.5 M $H_2SO_4$ | 396 $\mu g_{Ir}/cm^2$ | Adv. Funct. Mater. 34 (2024) 2400809 |
| $KIr_4O_8$ Nanowire | 266 | 109.6 mA·mg$^{-1}$ @1.53 $V_{RHE}$ | 159.6 mA·mg$^{-1}$ | 0.5 M $H_2SO_4$ | 0.281 mg/cm$^2$ | Adv. Mater. 36 (2024) 2402643 |
| $IrO_2$ Nano Ribbons | 205 | 2354.5 mA·mg$^{-1}$ @1.5 $V_{RHE}$ | / | 0.5 M $H_2SO_4$ | 0.23 $mg_{Ir}/cm^2$ | Nat. Commun. 14 (2023) 1248 |
| $TaO_x/IrO_2$ | 288 | 345 mA·mg$^{-1}$ @ 1.53 $V_{RHE}$ | 625.3 mA·mg$^{-1}$ | 0.1 M $HClO_4$ | 0.28 mg/cm$^2$ | Nat. Commun. 14 (2023) 5119 |
| $Ir_{0.3}Cr_{0.7}O_2$ | 255 | 81.258 mA·mg$^{-1}$ @1.5 $V_{RHE}$ | 353.4 mA·mg$^{-1}$ | 0.5 M $H_2SO_4$ | / | Int. J. Hydrogen Energy 48 (2023) 5402-5412 |
| Ir@$WO_x$ NW | / | 812 mA·$mg_{Ir}^{-1}$ @1.55 $V_{RHE}$ | 812 mA·$mg_{Ir}^{-1}$ | 0.5 M $H_2SO_4$ | 10.2 $\mu g_{Ir}/cm^2$ | Chem. Eng. J. 464 (2023) 142613 |
| Ir-$Co_3O_4$ | 236 | 3343.37 mA·$mg_{Ir}^{-1}$ @1.53 $V_{RHE}$ | 4477.7 mA·$mg_{Ir}^{-1}$ | 0.5 M $H_2SO_4$ | 0.018 $mg_{Ir}/cm^2$ | Nat. Commun. 13 (2022) 7754 |
| Amorphous Ir atomic clusters on $IrO_2$ | 296 | ~92 mA·mg$^{-1}$ @1.55 $V_{RHE}$ | ~92 mA·mg$^{-1}$ | 1.0 M $H_2SO_4$ | 0.25 mg/cm$^2$ | J. Power Sources 524 (2022) 231069 |
| Nanoneedles $Ir_xPb$ nanowire networks | 307 | 352 mA·mg$^{-1}$ @1.53 $V_{RHE}$ | 810.5 mA·mg$^{-1}$ | 0.1 M $HClO_4$ | / | J. Mater. Chem. A 10 (2022) 11196–11204 |
| $Ir_{0.7}W_{0.2}Sn_{0.1}O_x$ | 236 | 722.7 mA·$mg_{Ir}^{-1}$ @1.53 $V_{RHE}$ | / | 0.5 M $H_2SO_4$ | 0.3 mg/cm$^2$ | Small 18 (2022) 2203365 |
| $IrO_x/Ti_4O_7$ | 288 | 372 mA·mg$^{-1}$ @1.55 $V_{RHE}$ | 372 mA·mg$^{-1}$ | 0.1 M $HClO_4$ | 0.01 mg/cm$^2$ | Catal. Today 403 (2022) 19–27 |
| $Ir_{0.16}Co_{0.84}O_x$ | 262 | 1032.16 mA·mg$^{-1}$ @1.53 $V_{RHE}$ | / | 0.1 M $HClO_4$ | 51.91 μg/cm$^2$ | Electrochim. Acta 432 (2022) 141199 |
| Ir–$MnO_2$ | 218 | 766 mA·mg$^{-1}$ @1.53 $V_{RHE}$ | / | 0.5 M $H_2SO_4$ | / | Joule 5 (2021) 2164–2176 |
| $IrO_2$-B | 255~292 | 803 to 2779 mA·mg$^{-1}$ @1.53 $V_{RHE}$ | 1523.2 to 5271.6 mA·mg$^{-1}$ | 0.1 M $HClO_4$ | 51 to 5.1 $\mu g_{Ir}/cm^2$ | Sci. China Mater. 64 (2021) 2958–2966 |
| Ir/CP | 250 | 831.2 mA·$mg_{Ir}^{-1}$ @1.525 $V_{RHE}$ 6.8 A·$mg_{Ir}^{-1}$ @1.6 $V_{cell}$ | / | 0.5 M $H_2SO_4$ | 53.9 μg/cm$^2$ | Chem. Eng. J. 420 (2021) 127696 |
| $IrO_2$@TiN | 236 | 213 mA·mg$^{-1}$ @1.48 $V_{RHE}$ | 767.7 mA·mg$^{-1}$ | 0.5 M $H_2SO_4$ | / | Mater. Chem. Front. 5 (2021) 8047–8055 |
| Ir/$B_4C$ | 283 | 1100 mA·mg$^{-1}$ @1.54 $V_{RHE}$ | 1396.7 mA·mg$^{-1}$ | 0.1 M $HClO_4$ | 9.6 μg/cm$^2$ | J. Power Sources 512 (2021) 230506 |
| La–Ir NF | 263 | 375 mA·mg$^{-1}$ @1.55 $V_{RHE}$ | 375 mA·mg$^{-1}$ | 0.1 M $HClO_4$ | 0.2 mg/cm$^2$ | J. Mater. Chem. A 8 (2020) 12518–12525 |
| 30Ir/Au/CP | 318.7 | 440.5 mA·mg$^{-1}$ @1.9 $V_{cell}$ | / | 0.5 M $H_2SO_4$ | 0.008 mg/cm$^2$ | Applied Catalysis B: Environmental 283 (2021) |

| | | | | | | |
|---|---|---|---|---|---|---|
| | | | | | | 119596 |
| $IrO_2$ with dendrite-like nanostructures | 270 | 820 $mA \cdot mg^{-1}$ @1.55 $V_{RHE}$ | 820 $mA \cdot mg^{-1}$ | 0.5 M $H_2SO_4$ | 0.113 $mg/cm^2$ | Sustain. Energ. Fuels 4 (2020) 2462-2468 |
| (Mn, Ir)$O_2$:10F | 200 | 40 $mA \cdot mg^{-1}$ @1.45 $V_{RHE}$ | / | 0.5 M $H_2SO_4$ | 0.3 $mg/cm^2$ | ACS Catal. 9 (2019) 2134-2157 |
| Ir_VG | 300 | 2700 $mA \cdot mg^{-1}$ @1.53 $V_{RHE}$ | 5080.3 $mA \cdot mg^{-1}$ | 0.5 M $H_2SO_4$ | / | J. Mater. Chem. A 7 (2019) 20590–20596 |
| $IrO_2$/GCN | 278 | 1280 $mA \cdot mg^{-1}$ @1.6 $V_{RHE}$ | 507.2 $mA \cdot mg^{-1}$ | 0.5 M $H_2SO_4$ | 81 $\mu g/cm^2$ | Angew. Chem. Int. Ed. 58 (2019) 12540-12544 |
| Li-$IrSe_2$ | 220 | 66.16 $mA \cdot mg^{-1}$ @1.44 $V_{RHE}$ | / | 0.5 M $H_2SO_4$ | 250 $\mu g/cm^2$ | Angew. Chem. Int. Ed. 58 (2019) 14764-14769 |
| Ru@$IrO_x$ | 282 | 644.8 $mA \cdot mg^{-1}$ @1.56 $V_{RHE}$ | 512.7 $mA \cdot mg^{-1}$ | 0.05 M $H_2SO_4$ | 51 $\mu g/cm^2$ | Chem 5 (2019) 445-459 |
| 6H-$SrIrO_3$ | 248 | 75 $mA \cdot mg^{-1}$ @1.525 $V_{RHE}$ | 139.1 $mA \cdot mg^{-1}$ | 0.5 M $H_2SO_4$ | 900 $\mu g/cm^2$ | Nat. Commun. 9 (2018) 5236 |
| Mesoporous Ir nanosheets | 240 | 260 $mA \cdot mg^{-1}$ @1.5 $V_{RHE}$ | / | 0.5 M $H_2SO_4$ | / | J. Am. Chem. Soc. 140 (2018) 12434-12441 |